

# Exploring Energy Landscapes: Metrics, Pathways, and Normal-Mode Analysis for Rigid-Body Molecules

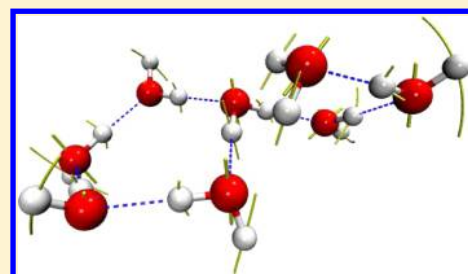
Victor Rühle,<sup>\*,†</sup> Halim Kusumaatmaja,<sup>†,‡</sup> Dwaipayan Chakrabarti,<sup>†,§</sup> and David J. Wales<sup>†</sup>

<sup>†</sup>Department of Chemistry, University of Cambridge, Lensfield Road, Cambridge CB2 1EW, United Kingdom

<sup>‡</sup>Department of Physics, Durham University, South Road, Durham DH1 3LE, United Kingdom

<sup>§</sup>School of Chemistry, University of Birmingham, Edgbaston, Birmingham B15 2TT, United Kingdom

**ABSTRACT:** We present new methodology for exploring the energy landscapes of molecular systems, using angle-axis variables for the rigid-body rotational coordinates. The key ingredient is a distance measure or metric tensor, which is invariant to global translation and rotation. The metric is used to formulate a generalized nudged elastic band method for calculating pathways, and a full prescription for normal-mode analysis is described. The methodology is tested by mapping the potential energy and free energy landscape of the water octamer, described by the TIP4P potential.



## I. INTRODUCTION

Simulations of molecular systems may involve a fully atomistic description, a coarse-grained approach that often relies upon the molecular shape, or a combination of the two. For atomistic potentials, a rigid-body description of a molecule can reduce the number of degrees of freedom, while retaining all the interatomic interactions. For example, rigid water molecules are commonly employed to speed up molecular dynamics simulations.<sup>1</sup> Applications of such rigid-body representations in computational science are wide-ranging, from crystal structure prediction of small organic molecules<sup>2–4</sup> to local rigidification of secondary structures in proteins and other biomolecules.<sup>5,6</sup> For simulations on longer length scales, coarse-grained descriptions are typically used, which may involve orientation-dependent potentials to describe nonspherical molecules with convex shapes.<sup>7–12</sup>

To represent an anisotropic molecule or interaction potential, six degrees of freedom are required (unless the molecule is linear): three for the translation of the center of mass and three for the orientation. The treatment of translational degrees of freedom is straightforward: they are usually represented by orthogonal Cartesian coordinates. The treatment of rotational degrees of freedom is, on the other hand, more cumbersome, and a number of possible approaches have been proposed, each with its own advantages and disadvantages. For example, the use of Euler angles suffers from singularities at the north and south poles, giving rise to the so-called gimbal lock problem;<sup>13</sup> quaternions are free from singularities but involve a four-parameter description with a unit norm constraint for three orientational degrees of freedom.<sup>13</sup>

Recent work has explored the use of angle-axis variables to represent the rigid-body rotational coordinates.<sup>9,14</sup> In the angle-axis representation, the orientation of a rigid body relative to a reference geometry is described by a rotation vector  $\mathbf{p}$ , which

denotes the axis of rotation, and the magnitude is the rotation angle around this axis. The main benefits of using this angle-axis representation in the context of energy landscape exploration are that singularities are avoided without involving additional parameters, constrained optimization is not required, it is straightforward to compute the first and second derivatives of the potential energy for a variety of intermolecular potentials,<sup>14</sup> and all calculations may be carried out in a single (laboratory) frame of reference (see Appendix A for possible frames of reference). In particular, derivatives with respect to the angle-axis coordinates are system-independent and can be programmed efficiently.<sup>14</sup>

In the present work, we further develop the angle-axis framework and present a number of advances in methodology. We derive a distance measure for angle-axis coordinates, which is invariant to overall translation and rotation. This measure is applied to define a convergence criterion for gradient based geometry optimization procedures to take into account the scaling problem arising from the presence of different types of coordinates. We next consider chain of state methods,<sup>15,16</sup> especially the doubly-nudged<sup>17</sup> elastic band (DNEB) approach,<sup>18,19</sup> which has proved to be particularly effective for finding transition states and constructing pathways between pairs of minima. Finally, we explain how to compute normal-mode frequencies in the angle-axis framework using a generalized curvilinear coordinate description.<sup>20</sup> These frequencies are needed to calculate thermodynamic properties within the harmonic superposition approximation.<sup>21–23</sup>

To provide proof of principle, we apply the angle-axis framework to characterize the potential and free energy landscape of a water cluster containing eight molecules, described by the TIP4P potential.<sup>1</sup> To map the energy

Received: May 16, 2013

Published: August 13, 2013

landscape, we first employ basin-hopping global optimization<sup>24</sup> to find the global minimum and construct a database of low energy minima. We then use a combination of the doubly-nudged<sup>17</sup> elastic band method<sup>18,19</sup> and hybrid eigenvector-following<sup>25,26</sup> to obtain minimum-transition state-minimum triplets. This procedure provides a global survey of the potential energy landscape, which we visualize using disconnectivity graphs.<sup>27,28</sup> Finally, we compute the free energy of the minima and transition states using the harmonic superposition approach<sup>21,23</sup> and construct the free energy disconnectivity graphs<sup>22,29</sup> at several representative temperatures.

## II. A DISTANCE METRIC FOR ANGLE-AXIS COORDINATES

Translational and rotational degrees of freedom have different physical dimensions, and care is thus needed to ensure they are treated on an equal footing. Furthermore, neither a rotation vector nor the difference between two rotation vectors, is invariant under overall rotation. In the following sections, we explain how to handle rotation vectors consistently in the context of minimization, chain of state methods, and normal-mode analysis.

First we show how to derive a distance measure, or equivalently a metric tensor, as the first step to tackle these problems. Lattmann<sup>30</sup> and Evans<sup>13</sup> have discussed the use of a metric tensor and distance measure for Euler angles and quaternions in previous work. We follow a generalized approach starting from an underlying atomistic description. Our discussion is based on the angle-axis formulation. However, the generalization to other descriptions of rotation is straightforward.

**A. Metric Tensor for Infinitesimal Distances.** We first consider a single rigid body, which is composed of  $N$  sites and associated masses,  $m_i$ , with Cartesian coordinates in the reference frame,  $\mathbf{x}_i$ . Sites are points in space (e.g., atoms), which define the shape of the rigid body. We denote the position of the rigid body by  $\mathbf{X}$ , which will usually correspond to the position of the center of mass or center of geometry relative to the origin. The rotation vector  $\mathbf{p}$  describes the orientation relative to the fixed reference geometry, and the rotation matrix  $\mathbf{R}$  is given by Rodrigues' rotation formula<sup>14</sup>

$$\mathbf{R} = \mathbf{I} + (1 - \cos \theta) \tilde{\mathbf{p}}\tilde{\mathbf{p}} + \sin \theta \tilde{\mathbf{p}} \quad (1)$$

where  $\mathbf{I}$  is a  $3 \times 3$  identity matrix, and  $\tilde{\mathbf{p}}$  is the skew-symmetric matrix obtained from  $\hat{\mathbf{p}} = \mathbf{p}/\theta$  with  $\theta = |\mathbf{p}|$ :

$$\tilde{\mathbf{p}} = \frac{1}{\theta} \begin{pmatrix} 0 & -p_3 & p_2 \\ p_3 & 0 & -p_1 \\ -p_2 & p_1 & 0 \end{pmatrix} \quad (2)$$

The position of site  $i$  in the lab frame is then

$$\mathbf{y}_i = \mathbf{X} + \mathbf{R}\mathbf{x}_i \quad (3)$$

It is convenient to define a weighted metric tensor

$$G_{\alpha\beta} = \sum_i w_i \frac{\partial \mathbf{y}_i}{\partial q_\alpha} \cdot \frac{\partial \mathbf{y}_i}{\partial q_\beta} \quad (4)$$

with the generalized coordinates  $\mathbf{q} = \{\mathbf{X}, \mathbf{p}\}$ . The choice of  $w_i$  depends on the property of interest: typically  $w_i = m_i$  for normal-mode analysis, or alternatively  $w_i = 1$  for the DNEB

procedure and the convergence criteria involved in geometry optimization. Inserting eq 3 into eq 4, we obtain

$$G_{\alpha\beta}^{\text{trans}} = W \delta_{\alpha\beta} \quad (5)$$

$$G_{\alpha\beta}^{\text{rot}} = \text{Tr}(\mathbf{R}_\alpha \mathbf{S} \mathbf{R}_\beta^T) \quad (6)$$

$$G_{\alpha\beta}^{\text{mix}} = (2W \mathbf{R}_\beta \mathbf{X}_w)_\alpha \quad (7)$$

where  $\text{Tr}$  stands for the trace and

$$\begin{aligned} W &= \sum_i w_i \\ \mathbf{X}_w &= \frac{1}{W} \sum_i w_i \mathbf{x}_i \\ \mathbf{R}_\alpha &= \partial \mathbf{R} / \partial p_\alpha \end{aligned} \quad (8)$$

$G_{\alpha\beta}^{\text{trans}}$  and  $G_{\alpha\beta}^{\text{rot}}$  are the components of the metric tensor that depend on translational and rotational degrees of freedom only, while  $G_{\alpha\beta}^{\text{mix}}$  contains the cross terms.  $\mathbf{S}$  is the weighted gyration tensor in the reference frame of the rigid body with

$$S_{\alpha\beta} = \sum_i w_i x_{i,\alpha} x_{i,\beta} \quad (9)$$

where  $x_{i,\alpha}$  is the  $\alpha (= x, y, z)$  component of the vector  $\mathbf{x}_i$ . Note that the mixing term  $G_{\alpha\beta}^{\text{mix}}$  vanishes for any consistent choice of  $w_i$  and rigid body mapping such that  $\sum w_i \mathbf{x}_i = \mathbf{0}$ , for example, if we take  $w_i = m_i$  and  $\mathbf{X}$  corresponds to the position of the center of mass, or alternatively if we take  $w_i = 1$  and use the center of geometry.

In the reference frame for the rigid body ( $\mathbf{p} = \mathbf{0}$ ) with  $w_i = m_i$ , the rotational part of the metric tensor is the familiar inertia tensor

$$I_{\alpha\beta} = \sum_i w_i (r_i^2 \delta_{\alpha\beta} - x_{i,\alpha} x_{i,\beta}) \quad (10)$$

Since  $G_{\alpha\beta}$  can be expressed purely in terms of the rigid body variables  $\mathbf{X}$  and  $\mathbf{p}$  and the gyration tensor  $\mathbf{S}$ , the general expression can be widely applied, for example, to the Stockmayer potential<sup>29</sup> and to coarse-grained molecular models that depend on orientation without an underlying site-site description.<sup>8,31</sup> In such cases, the gyration tensor is chosen directly to describe the shape of the underlying model.

**B. Finite Distances.** The metric tensor derived above can be used to calculate the length of an infinitesimal line element  $ds$ . However, for many applications, such as the chain of state methods discussed in section IV or for permutational alignment procedures,<sup>32</sup> a finite distance measure between two distinct orientations of a rigid body is required. In fact, there are at least two possible choices. First, we could use the arc length, which is the integral of  $ds$  over the shortest rotational separation connecting the two orientations in question. Alternatively, we could compute the direct finite distance measure, which is equivalent to the (weighted) sum of distances for the sites that decorate the rigid body. We focus on the latter approach in this subsection.

For two poses of a rigid body, distinguished by the subscripts 1 and 2, a (weighted) squared distance can be obtained by summing over the squared distances of the individual sites:

$$s_{12}^2 = \sum_i w_i (\mathbf{y}_{2,i} - \mathbf{y}_{1,i})^2 = \sum_i w_i \Delta \mathbf{y}_i^2 \quad (11)$$

Rewriting  $\Delta y_i$  as

$$\Delta y_i = X_2 - X_1 + R_2 x_i - R_1 x_i \equiv \Delta X + \Delta R x_i \quad (12)$$

and substituting eq 12 into eq 11, we obtain

$$\begin{aligned} s_{12}^2 &= \sum_i w_i (\Delta X + \Delta R x_i)^2 \\ &= \sum_i [w_i \Delta X^2 + w_i |\Delta R x_i|^2 + 2w_i \Delta X \cdot (\Delta R x_i)] \end{aligned} \quad (13)$$

The distance can therefore be separated into three contributions, namely translational, rotational, and mixed:

$$s_{12}^2 = s_{\text{trans}}^2 + s_{\text{rot}}^2 + s_{\text{mix}}^2 \quad (14)$$

with

$$s_{\text{trans}}^2 = \Delta X^2 W \quad (15)$$

$$s_{\text{rot}}^2 = \sum_i w_i |\Delta R x_i|^2 = \text{Tr}(\Delta R S \Delta R^T) \quad (16)$$

$$s_{\text{mix}}^2 = 2W \Delta X \cdot (\Delta R X_w) \quad (17)$$

Note that in the limit  $\Delta R \rightarrow 0$  and  $\Delta X \rightarrow 0$ , we can substitute  $X_2 = X_1 + dX$  and  $R_2 = R_1 + \sum R_{1,\alpha} dp_{1,\alpha}$  in eqs 15–17 and recover the metric tensors defined in eqs 5–7.

### III. GLOBAL OPTIMIZATION

In the previous section, we derived the metric tensor and distance measure for poses of a single rigid body. We now consider an arbitrary number of rigid bodies with generalized coordinates  $\mathbf{q} = \{q_\alpha\} = \{X_1, \dots, X_N, p_{1,1}, \dots, p_{N,N}\}$ . Since the coordinates for different rigid bodies are independent, the metric tensor for the full system is block diagonal, where each block corresponds to the metric tensor of an individual rigid body. The squared distance  $s^2$  between two different configurations is the sum of the squared distances  $s_i^2$  of the individual rigid bodies,  $I$ .

**A. Convergence Criterion for Local Energy Optimization.** An important step in basin-hopping global optimization<sup>24,33</sup> is to quench the system to a local potential energy minimum. We generally employ a modified limited-memory Broyden–Fletcher–Goldfarb–Shanno<sup>34</sup> (L-BFGS) algorithm for this purpose. A typical measure for convergence is the root-mean-square (RMS) gradient in the prevailing coordinate system. Here, we can now make use of the metric tensor derived above to calculate a coordinate independent measure for the RMS conditions.

The gradient of the potential energy with respect to the generalized coordinates  $\mathbf{q}$  is defined as  $\partial U / \partial \mathbf{q}$ . Following standard vector algebra in curvilinear coordinates,<sup>35</sup> we can define a scalar that is a dot product of the gradients as

$$u^2 = \sum_{\alpha\beta} \frac{\partial U}{\partial q_\alpha} G_{\alpha\beta}^{-1} \frac{\partial U}{\partial q_\beta}$$

$$\text{RMS} = \sqrt{u^2 / 6N} \quad (18)$$

where  $6N$  is the total number of degrees of freedom. We use the inverse metric tensor, rather than the metric tensor, because the energy gradients are dual vectors or covectors, and their components covary, rather than contra-vary, with a change of basis. For  $3N$  standard atomistic Cartesian coordinates, the metric tensor is the identity, and eq 18 simplifies to the usual RMS gradient  $(\sum_\alpha (\partial U / \partial x_\alpha)^2 / 3N)^{1/2}$ .

### IV. CHAIN OF STATE METHODS

Chain of state algorithms are an important class of methods for characterizing reaction pathways and rearrangement mechanisms.<sup>15,16</sup> In the present contribution, we focus on the doubly-nudged<sup>17</sup> elastic band<sup>18,19</sup> (DNEB) approach.

In previous work, Sheppard et al.<sup>36</sup> derived a generalized solid state NEB method to obtain pathways in crystalline systems, where the lattice vectors can change along the pathways. They derived a consistent treatment of the atomic coordinates and the lattice vectors, which describe different types of degrees of freedom. Here, we adopt an analogous approach to ref 36 and obtain a generalization of the (D)NEB method for a system of rigid bodies that involve translational and rotational coordinates.

The first step in the (D)NEB approach to characterize a transition path on the potential energy surface between two end points  $\mathbf{q}_0$  and  $\mathbf{q}_{N+1}$  is to make an initial guess for a set of images,  $\{\mathbf{q}_1, \mathbf{q}_2, \dots, \mathbf{q}_N\}$ , to trace out the path, where  $\mathbf{q}_i$  is the  $6N$ -dimensional ( $3N$  for atomistic systems) coordinate vector for image  $i$ . For a system of rigid bodies, the initial guess can be obtained via linear interpolation of the translational coordinates and spherical linear quaternion interpolation (SLERP)<sup>37</sup> of the rotational coordinates.

The images corresponding to the initial guess are then relaxed using the gradient that includes contributions from two components. The “true” gradient,  $\mathbf{g}_i$ , depends on the interaction potential alone, while the spring force component,  $\tilde{\mathbf{g}}_i$ , keeps the images roughly equidistant and is derived from the spring potential

$$V_i = \frac{k}{2} (s_{i,-}^2 - s_{i,+}^2) \quad (19)$$

where  $k$  is the spring constant and  $s_{i,-}$  and  $s_{i,+}$  are the distances to the  $i - 1$  (left) and  $i + 1$  (right) images of image  $i$ , respectively.

Using the true gradient and spring gradient without modification leads to corner-cutting (images are pulled away from the minimum energy path) and sliding-down problems (images slide down from barrier regions).<sup>18,19</sup> The key ingredient in NEB methods is the use of certain projections for the gradients based on the tangent  $\hat{\tau}_i$  along the path, hence the term *nudged*. We use the formulation in ref 19 to obtain  $\hat{\tau}_i$  based on the tangents to the left and to the right image,  $\tau_{i,-}$  and  $\tau_{i,+}$ , respectively. For an atomistic system, or equivalently the translational degrees of freedom of rigid bodies, the left and right tangents and distances  $s_\pm$  are given by

$$\begin{aligned} \tau_{i,\pm} &= \mathbf{q}_{i\pm 1} - \mathbf{q}_i \\ s_{i,\pm}^2 &= |\mathbf{q}_{i\pm 1} - \mathbf{q}_i|^2 \end{aligned} \quad (20)$$

Note that we define  $\tau_{i,-}$  with a different sign compared to ref 19.

The treatment of angle-axis coordinates on the same footing as translational coordinates for applications of the (D)NEB method to rigid-body systems is problematic. As such, it is less straightforward to define a suitable spring constant,  $k$ . Furthermore, the results can depend on the choice of reference frame, since angle-axis coordinates are not rotationally invariant. To alleviate these problems, we employ the distance measure in eq 14 for  $s_{i,\pm}$  and the left and right tangents can then be derived as

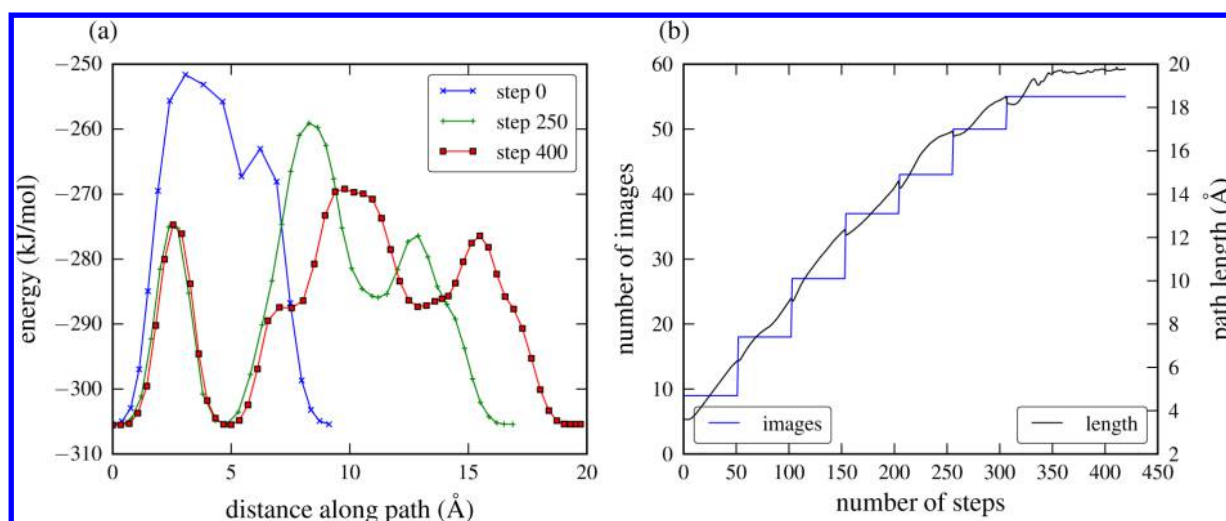


**Figure 1.** (a) DNEB pathways between the  $S_4$  and  $D_{2d}$  minima of the water octamer described by the TIP4P potential. (b) Path length defined using eq 11 and number of images versus number of optimization steps. The path length increases upon relaxing the DNEB to an approximate minimum energy path. The number of images is adapted every 50 steps to match a target image density of  $\rho = 3/\text{\AA}$ .

$$\tau_{i,\alpha,\pm} = \partial s_{i,\pm}^2 / \partial q_{i,\alpha} \quad (21)$$

for image  $i$  and degree of freedom  $\alpha$ . For the rotational degree of freedom, the derivative of the distance function is given by

$$\begin{aligned} \frac{1}{2} \frac{\partial s_i^2}{\partial q_{i,\alpha}} &= \frac{1}{2} \frac{\partial}{\partial q_{i,\alpha}} [\text{Tr}(\Delta \mathbf{R} \mathbf{S} \Delta \mathbf{R}^T) + \mathbf{X} \Delta \mathbf{R} \mathbf{X}_w] \\ &= -\text{Tr}(\mathbf{R}_{i,\alpha} \mathbf{S} \Delta \mathbf{R}^T) - \mathbf{X} \mathbf{R}_{i,\alpha} \mathbf{X}_w \end{aligned} \quad (22)$$

where we have used  $\mathbf{S} = \mathbf{S}^T$ . The derivatives with respect to the translational degrees of freedom can be obtained accordingly.

The first projection in both NEB and DNEB retains only the components of the true gradient that are perpendicular to the tangent vector  $\hat{\tau}_i$ :

$$\mathbf{g}_i^\perp = \mathbf{g}_i - (\mathbf{g}_i \cdot \hat{\tau}_i) \hat{\tau}_i \quad (23)$$

Removing the tangent part of the true gradient is numerically not sufficient to achieve equidistant images, and additional spring force components are required. The difference between NEB and DNEB lies in the nudging of the spring force. NEB only uses the spring force that is parallel to the path to avoid corner-cutting:

$$\tilde{\mathbf{g}}_i^{\text{NEB}} = k(s_{i,+} - s_{i,-}) \hat{\tau}_i \quad (24)$$

In some cases,<sup>17</sup> it can be beneficial to keep an additional perpendicular part of the spring gradient to improve the stability of the NEB. This approach leads to the DNEB method, which uses eq 24 for the parallel part and adds an additional perpendicular portion of the spring force

$$\tilde{\mathbf{g}}_i^{\text{DNEB}} = \tilde{\mathbf{g}}_i^{\text{NEB}} + \tilde{\mathbf{g}}^* \quad (25)$$

with

$$\tilde{\mathbf{g}}^* = \tilde{\mathbf{g}}_i^\perp - (\tilde{\mathbf{g}}_i^\perp \cdot \tilde{\mathbf{g}}_i^\perp) \tilde{\mathbf{g}}_i^\perp \quad (26)$$

$$\tilde{\mathbf{g}}_i^\perp = \tilde{\mathbf{g}}_i - (\tilde{\mathbf{g}}_i \cdot \hat{\tau}_i) \hat{\tau}_i \quad (27)$$

Several comments are in order:

(i) For rigid bodies, we find that it is particularly important to have a sufficiently large image density when optimizing the

path. Usually, the number of images is determined from the initial distance between the two end points. However, the length of the path can increase significantly upon optimizing the chain of images, and we have now implemented an adaptive number of images (D)NEB procedure. The total path length is calculated every  $M$  steps, and if the relative change in the number of images exceeds a certain threshold, a new path is generated with the appropriate image density by piecewise interpolation, using the images of the old path as supporting nodes. The reinterpolation with an adaptive number of images leads to a very robust DNEB method, which allows us to employ a minimal number of images to speed up the calculations. As indicated in Figure 1b, the length of the band changes upon reinterpolation. This change arises due to corner-cutting when the path is reinterpolated piecewise linearly. For high reinterpolation frequencies, it might be beneficial to perform higher order (e.g., spline) interpolation.

(ii) Results for the adaptive DNEB for rigid bodies are illustrated in Figure 1 for the  $S_4$  to  $D_{2d}$  transition of the water octamer cluster, described using the TIP4P potential.<sup>1</sup> We use a target image density of  $\rho = 3/\text{\AA}$  [using the distance formulation eq 14] with reinterpolation every 50 steps. The initial spring constant was  $k = 100 \text{ kJ/mol/\AA}^2$  and was adjusted every five steps, as described in ref 17. The chain of images was optimized using a modified L-BFGS algorithm.<sup>34</sup>

(iii) With the new distance measure for angle-axis coordinates, we can control the relative weight of the translational and rotational coordinates by scaling the gyration tensor. This control is useful for cases where the calculated distance does not properly reflect the change in the potential energy (i.e., for strongly directional interactions). In such cases, the energy profile along the path can become a narrow peak and render the (D)NEB procedure unstable. By increasing the gyration tensor, the weight of the distance calculation can be shifted toward the rotational coordinates, and a smoother energy profile can be obtained.

(iv) The distance formulation in eq 14 provides a direct distance measure rather than the arc length. This description is consistent with a formulation of (D)NEB based on all the molecular sites. However, for rotations of rigid bodies, it may lead to undesired cancellations of the spring forces. To illustrate



the problem, we depict in Figure 2 the scenario where the two neighboring images are rotated by exactly  $\pi$ . The torques that

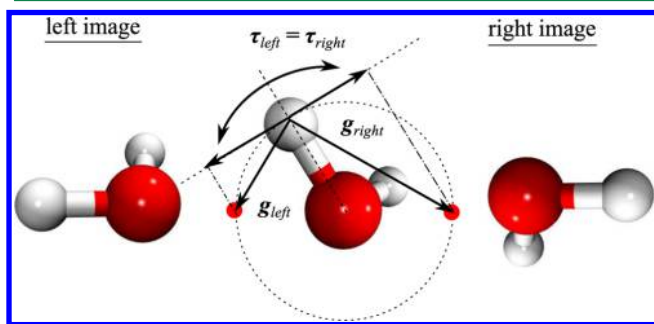


**Figure 2.** If a molecule in the left and right image is rotated exactly by  $\pi$ , the spring force on the middle molecule is zero. The torques that arise from the left and right spring force cancel out, while the remaining force vanishes due to the rigid-body constraints.

arise from the left and right spring forces cancel out, while the remaining force vanishes due to the rigid-body constraints. Such problems start to occur when a site in the left and right image is rotated by more than  $\pi/2$ .

(v) Both the NEB and (D)NEB approaches are compatible with our new distance measure for rigid bodies. For a NEB, additional constraints to remove the global translation and rotation of the system are required.<sup>38</sup> For DNEB, no such constraints are needed for clusters; however, it is not usually possible to converge tightly to the minimum energy path.<sup>39</sup> Since we refine transition state candidates using hybrid eigenvector-following,<sup>25,26</sup> we do not need to converge the band tightly, and therefore we generally choose the (D)NEB method over NEB.

(vi) Benchmarks comparing several optimization techniques<sup>39</sup> revealed that the fastest way to relax the band is L-BFGS, as in ref 17, with all images optimized simultaneously. In the present work, we again employ an L-BFGS procedure with line searches removed as implemented in the OPTIM program.<sup>40</sup> Since several gradient projections are involved, the objective function in a (D)NEB procedure is not well-defined, and it can be problematic to control the step size in the L-BFGS procedure. An alternative is the FIRE minimizer,<sup>41</sup> which uses only gradient information to determine the step size. In a few cases, we observed that FIRE, even though it converges slower than L-BFGS, can be more robust during the optimization process.

## V. ENERGY LANDSCAPES

**A. Potential Energy Landscapes.** One of the main applications for the doubly nudged elastic band method in energy landscape exploration is to construct a database of connected minima and transition states.<sup>42</sup> We start with a set of unconnected minima found during basin-hopping global optimization. We then use the DNEB method to connect pairs of minima. Images corresponding to local maxima in the DNEB are refined to transition states using hybrid eigenvector-following.<sup>25,26</sup> Once a transition state is found, two downhill approximate steepest-descent paths are traced, giving us a connected local minimum–transition state–local minimum triplet. A DNEB interpolation usually leads to multiple transition state candidates, and the downhill paths following the refinement routinely find new minima, different from the original pair we attempted to connect. Recursive use of this

procedure using the missing connection algorithm<sup>42</sup> provides us with a global survey of the potential energy landscape, which can be visualized using disconnectivity graphs.<sup>27,28</sup>

**B. Free Energy Landscapes.** To gain more insight into the thermodynamic properties of a system, it is convenient to construct free energy disconnectivity graphs<sup>22,23,29</sup> or calculate the heat capacity as a function of temperature.<sup>43,44</sup> The thermodynamic functions can be calculated approximately from the potential energy landscape using harmonic vibrational densities of states.<sup>21</sup> The partition function for a single minimum,  $Z_i(T)$ , at temperature  $T$  can then be written as

$$Z_i(T) = \frac{n_i^* \exp(-V_i/k_B T)}{(h\bar{\nu}_i/k_B T)^\kappa} \quad (28)$$

where  $V_i$  is the potential energy of minimum  $i$ , and  $n_i^*$  is the number of distinct permutation-inversion isomers.  $n_i^* \propto 1/h_i$ , where  $h_i$  is the order of the point group for the minimum.  $\bar{\nu}_i$  is the geometric mean of the positive normal-mode frequencies for minimum  $i$ , and  $\kappa$  is the number of vibrational degrees of freedom. We recall that the vibrational degrees of freedom exclude six zero eigenvalues in the normal mode calculation, which correspond to overall translation and rotation.

The harmonic free energy,  $F_i(T)$ , for minimum  $i$  is then calculated from the partition function via  $F_i = -k_B T \ln Z_i(T)$ . The free energy of a transition state can be defined in a similar way, except that the negative eigenvalue in the normal-mode frequency calculation is excluded ( $\kappa - 1$  vibrational modes).<sup>22</sup>

**C. Normal Mode Analysis.** The frequencies are calculated using a normal-mode analysis for the curvilinear coordinates  $\mathbf{q}$ ,<sup>20,45</sup> where  $\mathbf{q} = \{q_\alpha\} = \{X_1, \dots, X_N, p_1, \dots, p_2\}$ . The Lagrangian in curvilinear coordinates near a local minimum with energy  $V_{\min}$  up to harmonic order can be written as

$$L = \frac{1}{2} \dot{\mathbf{q}}^T \mathbf{G}^m \dot{\mathbf{q}} - \frac{1}{2} \mathbf{q}^T \mathbf{H} \mathbf{q} - V_{\min} \quad (29)$$

where  $\mathbf{G}^m$  is the mass weighted metric tensor [ $w_i = m_i$  in eq 4] and  $\mathbf{H}$  is the Hessian derived in curvilinear coordinates

$$H_{\alpha\beta} = \frac{\partial^2 V}{\partial q_\alpha \partial q_\beta} \quad (30)$$

The eigenmodes can be obtained by solving the generalized eigenvalue equation (see Appendix B)

$$\mathbf{H} - \lambda \mathbf{G}^m = \mathbf{0} \quad (31)$$

or, in other words, by calculating the eigenvalues of  $(\mathbf{G}^m)^{-1} \mathbf{H}$ . Note that if the metric tensor has zero eigenvalues,  $\mathbf{G}$  cannot be inverted. Instead, the pseudoinverse may be used.<sup>46</sup> This situation can arise in cases where there is a degeneracy in the potential energy, for example, arising from rotation about a local symmetry axis.

## VI. APPLICATIONS TO WATER CLUSTERS

The methods we have described in the previous sections are now applied to a cluster of eight water molecules interacting via the TIP4P potential.<sup>1</sup> We first perform a basin-hopping run with a temperature  $k_B T = 8$  kJ/mol, employing uniform rotational perturbations with angle  $\Delta\theta = 1.6$  (see Appendix C) and vanishing translational perturbations. Our initial database after basin-hopping included the two known lowest minima for this system.<sup>47,48</sup> The global minimum of the TIP4P water octamer has  $S_4$  symmetry with energy  $E = -305.51$  kJ/mol,

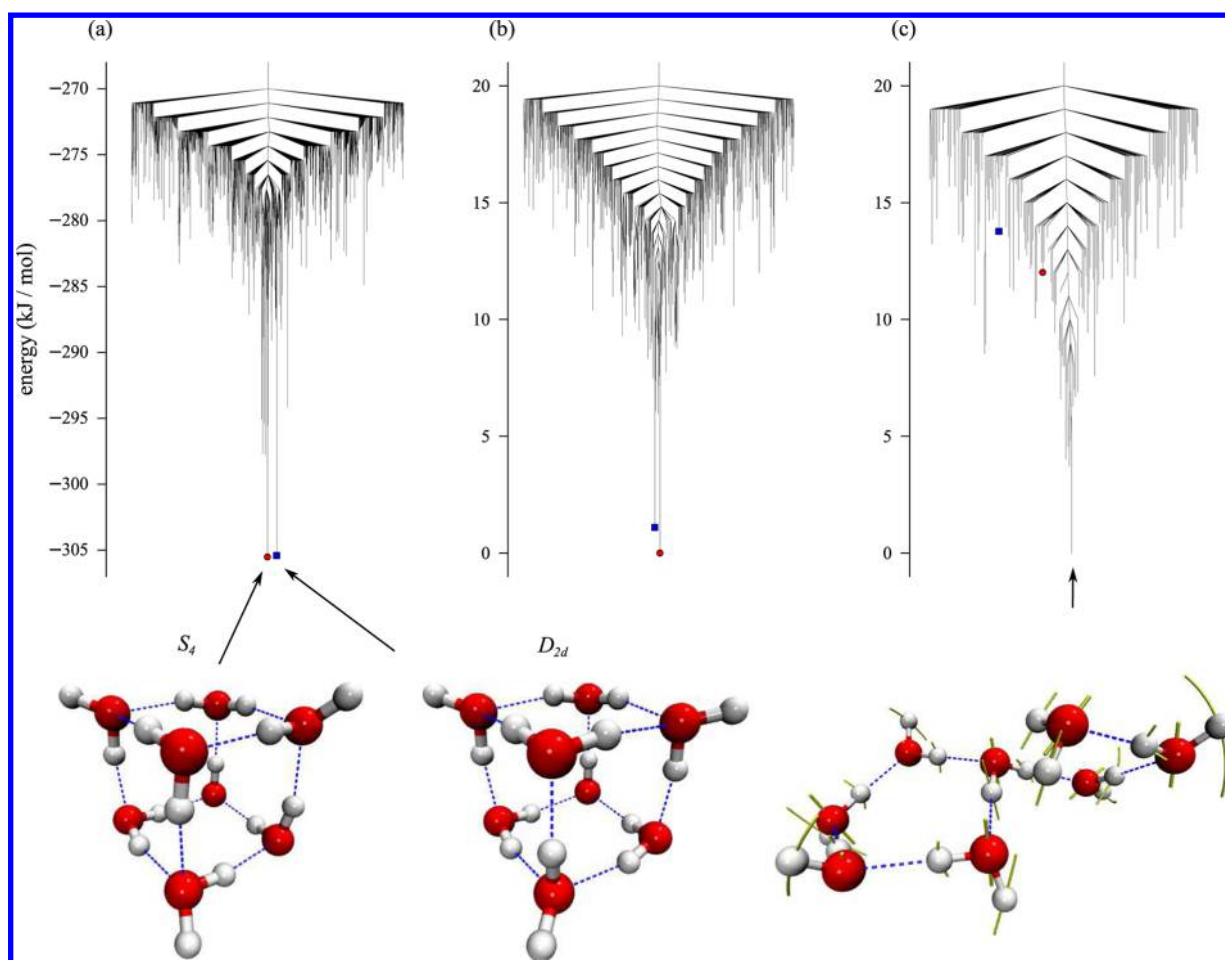


**Figure 3.** Disconnectivity graphs for a cluster of eight water molecules described by the TIP4P potential for the potential energy in part a and harmonic vibrational free energy at  $k_B T = 1.5$  kJ/mol in part b and  $k_B T = 2.5$  kJ/mol in part c. The lowest branch in the free energy disconnectivity graph (c) corresponds to a group of 312 minima. The yellow curves superimposed on the structure describe the normal mode with the smallest nonzero frequency of the lowest free energy minimum in that group.

while the second lowest minimum has a  $D_{2d}$  symmetry and  $E = -305.41$  kJ/mol.

The DNEB and hybrid eigenvector-following methods were then used recursively to construct a database of connected minima and transition states. We attempted to connect two randomly chosen minima in each DNEB optimization. This procedure often led to the discovery of new minima and the database therefore grew. Half of the connect runs were dedicated to connecting minima with energies below  $-275$  kJ/mol, which roughly corresponds to the highest lying transition state in the  $S_4$ – $D_{2d}$  transition path. In total, our database contained 4812 minima and 25 498 transition states.

To improve the sampling of low free energy regions for higher temperatures, we performed three 2 ns stochastic dynamics run at  $T = 270$  K using the GROMACS simulation package.<sup>49</sup> New minima were obtained by quenching from the resulting trajectory every 0.2 ps. Only minima where no molecules had dissociated were added to the database. Finally, we performed random double-ended connect runs for the 50 lowest free energy minima at  $k_B T = 2.5$  kJ/mol (this corresponds to a free energy band of roughly 5 kJ/mol). The potential energy disconnectivity graph shown in Figure 3a displays the minima that are connected to the global minimum via transition states lying below  $-270$  kJ/mol. In total, our database contained 6171 minima and 39 170 transition states.

The potential energy disconnectivity graph has been reported before.<sup>50</sup> Here, we present free energy disconnectivity graphs using the normal-mode analysis described in the previous section. We employ the harmonic superposition approximation to estimate the entropic contribution to the free energy, and we display the results for two representative temperatures:  $k_B T = 1.5$  kJ/mol ( $T = 180$  K) and  $k_B T = 2.5$  kJ/mol ( $T = 300$  K), as shown in Figure 3b and c, respectively. As before, we only display minima that are connected to the free energy global minimum by paths with transition states below 20 kJ/mol. To further improve the visualization of the free energy disconnectivity, we recursively regroup minima, where the barrier for the forward and backward transitions is smaller than  $k_B T$ .<sup>51–53</sup>

The free energy disconnectivity graphs reveal that the separation between the  $S_4$  and  $D_{2d}$  structures increases with increasing temperature. The vibrational modes of the two structures are in fact very similar, and the splitting originates from the different point group orders, which are 4 and 8 for  $S_4$  and  $D_{2d}$ , respectively. Upon increasing the temperature further, neither of these structures is the global free energy minimum (Figure 3c). Structures with fewer hydrogen bonds dominate the low free energy region, as they have much softer vibrational modes than the compact cluster structures.<sup>54</sup>

The validity of the harmonic approximation we have used to estimate the entropic contribution to the free energy could become problematic at higher temperatures, where well anharmonicity becomes important. In future work, we will compare the present results with parallel tempering calculations.

## VII. CONCLUSIONS

We have presented methodological advances for exploring the energy landscapes of molecular systems incorporating orientational degrees of freedom. Since translational and rotational degrees of freedom have different physical dimensions, special care is needed for a consistent treatment of both types of coordinates. We have derived a distance metric and metric tensor for angle-axis systems, which allow for such a treatment that is independent of the reference frame. The metric tensor was used to define a convergence criterion for geometry optimization, and the distance metric has been employed to derive a generalization of the (doubly) nudged elastic band approach. We have also considered normal-mode analysis in curvilinear coordinates to obtain vibrational frequencies, which are needed to estimate free energies based on the harmonic approximation. These results were then combined to explore the potential and free energy landscape of the water octamer, described by the TIP4P potential.

The theory has been developed in terms of the angle-axis representation of rotation. A generalization to other descriptions of rotation, such as quaternions or Euler angles, is straightforward since the derivations are based on the rotation matrix,  $\mathbf{R}$ . Furthermore, our methods can be implemented for rigid-body molecules, using center of mass coordinates, orientation, and the gyration tensor. This formulation is advantageous because the theory can be applied in exactly the same way for systems where there is no underlying atomistic model. Examples include orientation-dependent interaction potentials, which are widely used in mesoscopic simulations.<sup>7–12</sup>

All the methodology presented has been implemented in our public domain programs GMIN<sup>55</sup> and OPTIM,<sup>40</sup> and in a python package.<sup>56</sup>

## ■ APPENDIX A: CONVERTING THE GRADIENT BETWEEN FIXED AND MOVING REFERENCE FRAMES

When dealing with rigid bodies, there are two relevant frames of reference: the laboratory frame and the instantaneous frame. In the laboratory frame, the position of atom  $i$  in a rigid body with center of mass/geometry position  $\mathbf{X}$  and rotation matrix  $\mathbf{R}(\mathbf{p})$  is

$$\mathbf{y}_i = \mathbf{X} + \mathbf{R}\mathbf{x}_i \quad (\text{A1})$$

where  $\mathbf{x}_i$  are the fixed reference coordinates.

We now introduce the instantaneous frame. In this frame, we define the rigid body such that  $\mathbf{p} = \mathbf{0}$ , so that  $\mathbf{R} = \mathbf{I}$ , the identity matrix. Following eq 3, this definition implies  $\mathbf{y}_i = \mathbf{x}_i$  for  $\mathbf{X} = \mathbf{0}$ . In other words, we translate and rotate the reference coordinates to match the current site positions. This approach may seem inconvenient at first, but the advantages of this special frame of reference are that the angle-axis coordinates are orthogonal for the weighting  $w_i = m_i$ ; the rotational part of the metric tensor and energy gradients also correspond to the

familiar concepts of moment of inertia and torques in rigid body dynamics.

To convert a gradient given in the instantaneous frame, where we denote the rotation vector as  $\mathbf{P}$  for clarity, to that in the laboratory frame with rotation vector  $\mathbf{p}$ , we use the chain rule

$$\frac{\partial U}{\partial p_\alpha} = \sum_\beta \frac{\partial U}{\partial P_\beta} \frac{\partial P_\beta}{\partial p_\alpha} \quad (\text{A2})$$

A simple way to obtain  $\partial P_\beta / \partial p_\alpha$  is to compare the change in a vector  $\mathbf{r}$  under an infinitesimal rotation. In the instantaneous frame

$$d\mathbf{r} = \Theta \mathbf{r} \quad (\text{A3})$$

where

$$\Theta = \begin{pmatrix} 0 & -dP_3 & -dP_2 \\ dP_3 & 0 & -dP_1 \\ -dP_2 & dP_1 & 0 \end{pmatrix} \quad (\text{A4})$$

On the other hand, in the laboratory frame

$$d\mathbf{r} = \mathbf{R}_\alpha \mathbf{R}^{-1} dp_\alpha \mathbf{r} \quad (\text{A5})$$

Equating the two equations, eqs A3 and A5, we obtain

$$\begin{aligned} \frac{\partial P_1}{\partial p_\alpha} &= (\mathbf{R}_\alpha \mathbf{R}^{-1})_{32} \\ \frac{\partial P_2}{\partial p_\alpha} &= (\mathbf{R}_\alpha \mathbf{R}^{-1})_{13} \\ \frac{\partial P_3}{\partial p_\alpha} &= (\mathbf{R}_\alpha \mathbf{R}^{-1})_{21} \end{aligned} \quad (\text{A6})$$

The inverse gradient transformation from the laboratory to the instantaneous frame can be derived in the same way.

## ■ APPENDIX B: NORMAL MODE ANALYSIS IN CURVILINEAR COORDINATES

Here, we derive the generalized eigenvalue equation, eq 31. Inserting the Lagrangian defined by eq 29 into the Euler–Lagrange equation, we obtain

$$\begin{aligned} \frac{\partial L}{\partial q_\alpha} - \frac{d}{dt} \frac{\partial L}{\partial \dot{q}_\alpha} &= 0 \\ H_{\alpha\beta} q_\beta + \frac{d}{dt} G_{\alpha\beta}^m \dot{q}_\beta &= 0 \end{aligned} \quad (\text{B1})$$

where we have evaluated the metric tensor  $G_{\alpha\beta}^m$  at the corresponding minimum energy configuration and neglected changes as we move away from that particular point. This approximation is made so that the normal-mode analysis does not depend on the amplitude of the oscillation. Assuming that the oscillation has the usual form  $\mathbf{q} = \mathbf{A}q^{i\omega t}$ , where  $\mathbf{A}$  is the amplitude vector,  $\omega$  is the frequency, and  $\lambda = \omega^2$  is the eigenvalue, we obtain

$$(H_{\alpha\beta} q_\beta - \lambda G_{\alpha\beta}^m q_\beta) = 0 \quad (\text{B2})$$

This equation is equivalent to the generalized eigenvalue problem, eq 31. A more detailed discussion can be found in ref 20.



## ■ APPENDIX C: UNIFORM STEP TAKING

Another subtle issue for global optimization within the angle-axis framework is step-taking. In almost all basin-hopping structure perturbations, one generally wants to take a rotational step that is uniform. However, directly displacing angle-axis coordinates by a random value does not lead to uniform random rotational displacements. In particular, for increasing  $|\mathbf{p}|$ , this procedure leads to rotations mainly around the current rotation vector  $\mathbf{p}$ .

To illustrate this effect, consider an angle-axis vector  $\mathbf{p} = (p, 0, 0)$ , with  $p \gg 1$ . A displacement of  $\Delta p \ll p$  in the  $x$  direction of the angle-axis vector corresponds to an additional rotation  $\Delta p$  along the  $(1, 0, 0)$  axis. On the other hand, the same displacement  $\Delta p$  in the  $y$  (or  $z$  direction) results in a small shift in the rotation axis to  $(1 - (\Delta p)^2/2p^2, \Delta p/p, 0)$ , and an additional rotation of  $(\Delta p)^2/2p$ .

A uniform random rotation can be generated by first taking a uniformly distributed rotation axis,  $\hat{\mathbf{p}}$ , and choosing a rotation angle  $\theta$  according to the probability distribution<sup>57</sup>

$$p(\theta) \propto \frac{1}{\pi} \sin^2(\theta/2), \theta \in [0, \pi] \quad (\text{C1})$$

In practice, efficient algorithms have been developed to directly generate uniform distributed random rotations: see ref 58 for quaternions and ref 59 for rotation matrices.

In some applications, one may also prefer to generate a random rotational displacement with a maximum rotation angle  $\theta_{\max}$ . To achieve this goal, we independently choose a random rotation axis  $\hat{\mathbf{p}}$  and an angle  $\theta \in [0, \theta_{\max}]$  from the distribution in eq C1.

## ■ AUTHOR INFORMATION

### Corresponding Author

\*E-mail: vr274@cam.ac.uk.

### Notes

The authors declare no competing financial interest.

## ■ ACKNOWLEDGMENTS

We gratefully acknowledge Dr. Jacob Stevenson and James Farrell for stimulating discussions. This research was funded by EPSRC Programme grant EP/I001352/1 and a European Research Council Advanced Grant.

## ■ REFERENCES

- (1) Jorgensen, W. L.; Chandrasekhar, J.; Madura, J. D.; Impey, R. W.; Klein, M. L. Comparison of simple potential functions for simulating liquid water. *J. Chem. Phys.* **1983**, *79*, 926–935.
- (2) Price, S. L.; Leslie, M.; Welch, G. W. A.; Habgood, M.; Price, L. S.; Karamertzanis, P. G.; Day, G. M. Modelling organic crystal structures using distributed multipole and polarizability-based model intermolecular potentials. *Phys. Chem. Chem. Phys.* **2010**, *12*, 8478.
- (3) Kazantsev, A. V.; Karamertzanis, P. G.; Adjiman, C. S.; Pantelides, C. C.; Price, S. L.; Galek, P. T.; Day, G. M.; Cruz-Cabeza, A. J. Successful prediction of a model pharmaceutical in the fifth blind test of crystal structure prediction. *Int. J. Pharm.* **2011**, *418*, 168–178.
- (4) Day, G. M. Current approaches to predicting molecular organic crystal structures. *Crystallogr. Rev.* **2011**, *17*, 3–52.
- (5) Kusumaatmaja, H.; Whittleston, C. S.; Wales, D. J. A Local Rigid Body Framework for Global Optimization of Biomolecules. *J. Chem. Theory Comput.* **2012**, *8*, 5159–5165.
- (6) Dupuis, L.; Mousseau, N. Understanding the EF-hand closing pathway using non-biased interatomic potentials. *J. Chem. Phys.* **2012**, *136*, 035101.
- (7) Stockmayer, W. H. Second Virial Coefficients of Polar Gas Mixtures. *J. Chem. Phys.* **1941**, *9*, 863–870.
- (8) Gay, J. G.; Berne, B. J. Modification of the overlap potential to mimic a linear site–site potential. *J. Chem. Phys.* **1981**, *74*, 3316–3319.
- (9) Wales, D. J. The energy landscape as a unifying theme in molecular science. *Philos. Trans. R. Soc. London, Ser. A* **2005**, *363*, 357–377.
- (10) Hagan, M. F.; Chandler, D. Dynamic Pathways for Viral Capsid Assembly. *Biophys. J.* **2006**, *91*, 42–54.
- (11) Glotzer, S. C.; Solomon, M. J. Anisotropy of building blocks and their assembly into complex structures. *Nat. Mater.* **2007**, *6*, 557–562.
- (12) Ouldridge, T. E.; Louis, A. A.; Doye, J. P. K. Structural, mechanical, and thermodynamic properties of a coarsegrained DNA model. *J. Chem. Phys.* **2011**, *134*, 085101.
- (13) Evans, D. J. On the representation of orientation space. *Mol. Phys.* **1977**, *34*, 317–325.
- (14) Chakrabarti, D.; Wales, D. J. Simulations of rigid bodies in an angle-axis framework. *Phys. Chem. Chem. Phys.* **2009**, *11*, 1970.
- (15) Elber, R.; Karplus, M. A method for determining reaction paths in large molecules: Application to myoglobin. *Chem. Phys. Lett.* **1987**, *139*, 375–380.
- (16) Czerninski, R.; Elber, R. Reaction path study of conformational transitions in flexible systems: Applications to peptides. *J. Chem. Phys.* **1990**, *92*, 5580–5601.
- (17) Trygubenko, S. A.; Wales, D. J. A doubly nudged elastic band method for finding transition states. *J. Chem. Phys.* **2004**, *120*, 2082–2094.
- (18) Henkelman, G.; Uberuaga, B. P.; Jónsson, H. A climbing image nudged elastic band method for finding saddle points and minimum energy paths. *J. Chem. Phys.* **2000**, *113*, 9901–9904.
- (19) Henkelman, G.; Jónsson, H. Improved tangent estimate in the nudged elastic band method for finding minimum energy paths and saddle points. *J. Chem. Phys.* **2000**, *113*, 9978–9985.
- (20) Pesonen, J.; Henriksson, K. O. E.; López-Blanco, J. R.; Chacón, P. Normal mode analysis of molecular motions in curvilinear coordinates on a non-Eckart body-frame: an application to protein torsion dynamics. *J. Math. Chem.* **2012**, *50*, 1521–1549.
- (21) Wales, D. J. Coexistence in small inert gas clusters. *Mol. Phys.* **1993**, *78*, 151–171.
- (22) Evans, D. A.; Wales, D. J. Free energy landscapes of model peptides and proteins. *J. Chem. Phys.* **2003**, *118*, 3891–3897.
- (23) Strodel, B.; Wales, D. J. Free energy surfaces from an extended harmonic superposition approach and kinetics for alanine dipeptide. *Chem. Phys. Lett.* **2008**, *466*, 105–115.
- (24) Wales, D. J.; Doye, J. P. K. Global Optimization by Basin-Hopping and the Lowest Energy Structures of Lennard-Jones Clusters Containing up to 110 Atoms. *J. Phys. Chem. A* **1997**, *101*, 5111–5116.
- (25) Munro, L. J.; Wales, D. J. Defect migration in crystalline silicon. *Phys. Rev. B* **1999**, *59*, 3969–3980.
- (26) Henkelman, G.; Jónsson, H. A dimer method for finding saddle points on high dimensional potential surfaces using only first derivatives. *J. Chem. Phys.* **1999**, *111*, 7010–7022.
- (27) Becker, O. M.; Karplus, M. The topology of multidimensional potential energy surfaces: Theory and application to peptide structure and kinetics. *J. Chem. Phys.* **1997**, *106*, 1495–1517.
- (28) Wales, D. J.; Miller, M. A.; Walsh, T. R. Archetypal energy landscapes. *Nature* **1998**, *394*, 758–760.
- (29) Krivov, S. V.; Karplus, M. Free energy disconnectivity graphs: Application to peptide models. *J. Chem. Phys.* **2002**, *117*, 10894–10903.
- (30) Lattman, E. E. Optimal sampling of the rotation function. *Acta Crystallogr., Sect. B* **1972**, *28*, 1065–1068.
- (31) Paramonov, L.; Yaliraki, S. N. The directional contact distance of two ellipsoids: Coarse-grained potentials for anisotropic interactions. *J. Chem. Phys.* **2005**, *123*, 194111.
- (32) Wales, D. J.; Carr, J. M. Quasi-Continuous Interpolation Scheme for Pathways between Distant Configurations. *J. Chem. Theory Comput.* **2012**, *8*, 5020–5034.



- (33) Li, Z.; Scheraga, H. A. Monte Carlo-minimization approach to the multiple-minima problem in protein folding. *Proc. Natl. Acad. Sci. U.S.A.* **1987**, *84*, 6611–6615.
- (34) Byrd, R. H.; Lu, P.; Nocedal, J.; Zhu, C. A Limited Memory Algorithm for Bound Constrained Optimization. *SIAM J. Sci. Comput.* **1995**, *16*, 1190.
- (35) Riley, K. F.; Hobson, M. P.; Bence, S. J. *Mathematical Methods for Physics and Engineering: A Comprehensive Guide*, 3rd ed.; Cambridge University Press: New York, 2006; pp 763–725.
- (36) Sheppard, D.; Xiao, P.; Chemelewski, W.; Johnson, D. D.; Henkelman, G. A generalized solid-state nudged elastic band method. *J. Chem. Phys.* **2012**, *136*, 074103.
- (37) Shoemake, K. Animating rotation with quaternion curves. *SIGGRAPH Comput. Graph.* **1985**, *19*, 245–254.
- (38) Jónsson, H.; Mills, G.; Jacobsen, K. W. *Classical and Quantum Dynamics in Condensed Phase Simulations*; World Scientific: Singapore, 1998; pp 385–404.
- (39) Sheppard, D.; Terrell, R.; Henkelman, G. Optimization methods for finding minimum energy paths. *J. Chem. Phys.* **2008**, *128*, 134106.
- (40) Wales, D. J. OPTIM: A program for optimizing geometries and calculating pathways. <http://www-wales.ch.cam.ac.uk/software.html>.
- (41) Bitzek, E.; Koskinen, P.; Gähler, F.; Moseler, M.; Gumbusch, P. Structural Relaxation Made Simple. *Phys. Rev. Lett.* **2006**, *97*, 170201.
- (42) Wales, D. J. Discrete path sampling. *Mol. Phys.* **2002**, *100*, 3285–3305.
- (43) Bogdan, T. V.; Wales, D. J.; Calvo, F. Equilibrium thermodynamics from basin-sampling. *J. Chem. Phys.* **2006**, *124*, 044102.
- (44) Wales, D. J.; Bogdan, T. V. Potential Energy and Free Energy Landscapes. *J. Phys. Chem. B* **2006**, *110*, 20765–20776.
- (45) Banerjee, A.; Adams, N. P. On coordinate transformations in steepest descent path and stationary point locations. *Int. J. Quantum Chem.* **1992**, *43*, 855–871.
- (46) Ben-Israel, A.; Greville, T. N. E. *Generalized Inverses: Theory and Applications*, 2nd ed.; Springer: New York, 2003.
- (47) Tsai, C. J.; Jordan, K. D. Use of the histogram and jump-walking methods for overcoming slow barrier crossing behavior in Monte Carlo simulations: Applications to the phase transitions in the (Ar)<sub>13</sub> and (H<sub>2</sub>O)<sub>8</sub> clusters. *J. Chem. Phys.* **1993**, *99*, 6957–6970.
- (48) Tharrington, A. N.; Jordan, K. D. Parallel-Tempering Monte Carlo Study of (H<sub>2</sub>O)<sub>n</sub> = 6–9. *J. Phys. Chem. A* **2003**, *107*, 7380–7389.
- (49) Hess, B.; Kutzner, C.; van der Spoel, D.; Lindahl, E. GROMACS 4: Algorithms for highly efficient, load-balanced, and scalable molecular simulation. *J. Chem. Theory Comput.* **2008**, *4*, 435–447.
- (50) James, T.; Wales, D. J.; Hernández Rojas, J. Energy landscapes for water clusters in a uniform electric field. *J. Chem. Phys.* **2007**, *126*, 054506.
- (51) Carr, J. M.; Wales, D. J. Global optimization and folding pathways of selected  $\alpha$ -helical proteins. *J. Chem. Phys.* **2005**, *123*, 234901.
- (52) Carr, J. M.; Wales, D. J. Folding Pathways and Rates for the Three-Stranded  $\beta$ -Sheet Peptide Beta3s using Discrete Path Sampling. *J. Phys. Chem. B* **2008**, *112*, 8760–8769.
- (53) Carr, J. M.; Wales, D. J. Refined kinetic transition networks for the GB1 hairpin peptide. *Phys. Chem. Chem. Phys.* **2009**, *11*, 3341–3354.
- (54) Wales, D. J. *Energy Landscapes: Applications to Clusters, Biomolecules and Glasses*; Cambridge University Press: New York, 2004; pp 434–529.
- (55) Wales, D. J. GMIN: A program for basin-hopping global optimization, basin-sampling, and parallel tempering. <http://www-wales.ch.cam.ac.uk/software.html>.
- (56) Python Energy Landscape Explorer. <http://github.com/pele-python/pele>.
- (57) Miles, R. E. On Random Rotations in  $R^3$ . *Biometrika* **1965**, *52*, 636–639.
- (58) Shoemake, K. In *Graphics Gems III*; Kirk, D., Ed.; Academic Press: New York, 1992; pp 124–132.
- (59) Arvo, J. In *Graphics Gems III*; Kirk, D., Ed.; Academic Press: New York, 1992; pp 117–120.